Pressure-tuned plethora of ferroelectric phases in $CuInP_2S_6$

Sambridhi Shah,[1] Pegah Mohammadi,[2] Bess G. Singidas,[3] Kevin A. Smith,[1] Yanhong Gu,[1] Luther J. Langston,[1] Brian Taylor,[1] Ryan P. Siebenaller,[4,5] Michael A. Susner,[5] Sang-Wook Cheong,[6,7] Hirokazu Kadobayashi,[8] Roland V. Sarmago,[3] Zhenxian Liu,[9] Takahiro Matsuoka*,[3,10,11] Sobhit Singh*,[2,12] and Janice L. Musfeldt[1,13,*]

[1]*Department of Chemistry, University of Tennessee, Knoxville, Tennessee 37996, USA*
[2]*Department of Mechanical Engineering, University of Rochester, Rochester, New York 14627, USA*
[3]*National Institute of Physics, College of Science, University of the Philippines-Diliman, Quezon City 1101, Philippines*
[4]*Department of Materials Science and Engineering, The Ohio State University, Columbus, OH 43210, USA*
[5]*Materials and Manufacturing Directorate, Air Force Research Laboratory, Wright-Patterson Air Force Base, Ohio 45433, USA*
[6]*Department of Physics and Astronomy, Rutgers University, Piscataway, New Jersey 08854 USA*
[7]*Keck Center for Quantum Magnetism, Rutgers University, Piscataway, New Jersey 08854 USA*
[8]*Japan Synchrotron Radiation Research Institute (JASRI), Sayo, Hyogo 679-5198, Japan*
[9]*Department of Physics, University of Illinois Chicago, Chicago, Illinois 60607-7059, USA*
[10]*Center for Science and Technology under Extreme Conditions, Osaka University, Toyonaka, Osaka 5608531, Japan*
[11]*Japan Synchrotron Radiation Research Institute (JASRI), Sendai, Miyagi 980-8577, Japan*
[12]*Material Science Program, University of Rochester, Rochester, New York 14627, USA*
[13]*Department of Physics and Astronomy, University of Tennessee, Knoxville, Tennessee 37996, USA*

(Dated: January 7, 2026)

Abstract

Layered chalcogenides like $CuInP_2S_6$ are room temperature ferroelectrics. Modest compression even increases the electric polarization, raising questions about the origin of this unusual trend and other properties under pressure. In this work, we combine synchrotron-based infrared and Raman scattering spectroscopies, x-ray diffraction, and resistivity measurements with first-principles calculations of the lattice dynamics and energy landscape to unravel the influence of pressure on symmetry, polarization, and metallicity. We uncover a remarkable series of phase transitions across a series of polar space groups: monoclinic Cc → trigonal $P31c$ (prismatic sulfur) → $P31c$ (octahedral sulfur). True metallicity develops above 63 GPa, significantly higher than in related MPS$_3$ materials (M = Mn, Co, Fe, Ni), offering a picture of competing states of matter that is different than previously supposed. Detailed examination of pressure trends within the Cc phase also reveals phonon lifetime changes and streaking of satellite x-ray peaks that correlate with the maximum polarization. We discuss these tendencies in terms of Cu^+ ion migration, phase formation, and the overall energy landscape. Our findings place the high pressure behavior of $CuInP_2S_6$ on a firm foundation and pave the way for the development of structure-property relations in this family of complex chalcogenides.

* Corresponding authors: tmatsuoka@up.edu.ph; s.singh@rochester.edu; musfeldt@tennessee.edu

INTRODUCTION

Concepts of close-packing combined with conventional wisdom often holds that common three-dimensional solids tend toward the cubic state under compression.[1,2] Layered chalcogenides deviate from this familiar trend because pressure acts upon bond lengths and angles as well as the van der Waals gap and c/a ratio to yield many different states of matter.[3] Even so, there is a general proclivity toward more symmetric space groups and low spin configurations under compression. Thus, it is a real surprise when pressure is able to (i) trigger the development of properties such as ferroelectricity that depend upon the absence of inversion and mirror planes, (ii) touch off the development of new polar states, or (iii) increase the magnitude of the polarization in a given state.[4] The latter was recently reported in $CuInP_2S_6$, a bimetallic member of the MPX_3 family of materials (M = Mn, Fe, Ni, Zn, Co, Cd; X = S, Se) known for chemical tunability and sensitivity to external stimuli.[5–8] Although the details differ, it has been found that polarization more than doubles in response to relatively small pressures - on the order of a few GPa - before being quenched again across a structural distortion.[9–11] This is a curious response to be sure and raises questions about exactly why polarization is so dependent upon pressure in this system and whether it can be replicated or enhanced. Examination of the properties and crystal structure offers some clues. $CuInP_2S_6$ hosts a Cc space group [Fig. 1**a**] and intrinsic ferroelectricity at room temperature.[5,6,8,12–14] Key to the development of out-of-plane polarization is an asymmetric displacement of Cu^+ ions.[15–19] Control over the Cu concentration during crystal growth has always been challenging, and there is plenty of evidence in the form of $CuBiP_2Se_6$[20] and $CuCrP_2S_6$[21–23] to indicate that these Cu centers are mobile. This makes it difficult to determine intrinsic properties, and questions persist as to the sequence of critical pressures, symmetry of the space groups, and development of metallicity in this system.[7,9,11,24] Resolving these issues is crucial to establishing the true potential of this family of layered ferroelectrics.

In this work, we combine high pressure synchrotron-based infrared and Raman scattering spectroscopies, x-ray scattering, and electrical transport with a detailed symmetry analysis and first-principles calculations of the lattice dynamics and energy landscape to establish the progression of structural phase transitions $Cc \rightarrow P31c$ (prismatic) $\rightarrow P31c$ (octahedral sulfur sublattice) and development of metallicity above 63 GPa. Remarkably, all three of

these phases are polar, although the ensuing transitions restore certain symmetry elements, increase overall crystal symmetry, and diminish polarization. At the same time, we explore the compression-induced polarization increase within the Cc phase and discuss Cu ion migration in terms of phonon dynamics and lifetime trends, phase formation, and a detailed analysis of the energy landscape. In addition to bringing together a remarkably powerful and versatile set of techniques for revealing the pressure-driven phases of a layered ferroelectric, our work opens the door to similar approaches in other complex chalcogenides as well as opportunities for the development of structure–property relationships. These findings will advance a number of allied fields, including those in which property descriptors for A- and B-site substitution help integrate $CuInP_2S_6$-based ferroelectrics into functional devices.

RESULTS AND DISCUSSION

Vibrational properties of $CuInP_2S_6$ at ambient condition

Figure 1**b,c** displays the vibrational properties of $CuInP_2S_6$ at room temperature and ambient pressure conditions. We assign the Raman and infrared spectral features according to a symmetry analysis and complementary lattice dynamics calculations.[8] This system hosts a polar Cc space group under these conditions, which means that it has a single mirror plane perpendicular to the b axis. Group theory reveals $\Gamma_{vib} = 28\mathrm{A}' + 29\ \mathrm{A}''$, where the nondegenerate A′ and A″ optical modes are both Raman- and infrared-active.[8,25] Not all of these features are observed in Fig. 1**b,c** due to weak intensities, crystal orientation, or overlap with stronger modes. We resolve 15 peaks in the Raman scattering response and 18 peaks in the infrared absorbance. We further point out that although both A′ and A″ phonons meet the selection rules, they are not active with equal intensities. This is why it is useful to measure both Raman scattering and infrared absorbance. A summary of calculated and experimental phonon mode frequencies, symmetries, and displacement patterns is given in Tables S1 and S2, Supplementary Information. In particular, the A′ and A″ phonon modes near 31 and 69 cm^{-1} are in-plane and out-of-plane Cu-S vibrations, the A′ mode at 103 cm^{-1} is a rigid out-of-plane In-P-S displacement, the A″ peak at 111 cm^{-1} is an in-plane Cu-P + out-of-plane S vibration, and the A′ and A″ features at 543 and 553 cm^{-1} are in-plane P-P-S vibrations. Taken together, these findings put the mode assignments and overall vibration

pattern of $CuInP_2S_6$ on a firm foundation.

Vibrational properties of $CuInP_2S_6$ under pressure

Figure 2 summarizes the vibrational properties of $CuInP_2S_6$ as a function of pressure. While there is prior high pressure Raman scattering work on this system,[7,10,11,25,26] the infrared response is entirely unexplored - primarily due to the overall low signal level, which we address using accelerator-based techniques. This is one of the distinctions of our work. In addition to revealing phonon behavior, infrared spectroscopy is sensitive to the development of metallicity.[3,27–29] As usual, we identify critical pressures (P_C's) by the appearance or disappearance of peaks, the development of different peak-splitting patterns, frequency shifts, and line width changes.[28,29] These measurements reveal a sequence of pressure-driven structural phase transitions with two critical pressures (P_C's) and three different phases. Analysis of the frequency vs. pressure data reveals the first critical pressure ($P_{C,1}$) at approximately 4.6 GPa. In the Raman scattering response, this transition is characterized by (i) a softening of 31 cm^{-1} A′ symmetry mode, (ii) disappearance of a number of features between 68 and 445 cm^{-1}, (iii) a frequency shift in the 111 cm^{-1} peak, and (iv) the appearance of new modes at 203 and 276 cm^{-1}. In the infrared absorbance, $P_{C,1} = 4.6$ GPa takes place with (i) the disappearance of peaks at 80, 160, 163, and 572 cm^{-1}, (ii) the appearance of a feature near 230 cm^{-1}, and (iii) the softening of phonon modes near 300 cm^{-1}. The pressure-driven Cc → HP-I transition clearly coincides with an overall decrease in the number of phonon modes and a restoration of symmetry. But as we shall see below, both our first principles calculations and group-subgroup analysis are inconsistent with a transition to a nonpolar state like the previously reported $P\bar{3}1m$[9,10,30] or $P\bar{3}1c$.[11,15]

Examination of the frequency vs. pressure trends reveals that $CuInP_2S_6$ hosts an additional structural phase transition around $P_{C,2} = 12$ GPa. The appearance of a new peak at 93 cm^{-1} and the disappearance of a mode near 156 cm^{-1} in the Raman scattering spectrum combined with the disappearance of the 320 cm^{-1} mode in the infrared absorbance suggest that the symmetry changes across $P_{C,2}$. Interestingly, our first principle calculations predict that the polar $P31c$ phase is enthalpically favored in this pressure regime, although there are several competing low-energy metastable trigonal structures ($P\bar{3}$, $P312$, $P31c$, and $P\bar{3}1c$)

that may be stabilized at finite temperatures due to entropic contributions [Fig. 4**a**]. We discuss the overall symmetry progression and propose a resolution to this structural puzzle below.

Finally, we point out that many of the MPX_3 materials (M = Mn, Co, Ni; X = S, Se) display insulator-to-metal transitions under compression.[3] The Cd analog is, of course, different due to the filled $4d$ orbitals which gives a band-like (rather than Mott) character to the system.[31] Bimetallic analogs like $CuInP_2S_6$ are anticipated to host insulator-to-metal transitions as well, although they can be tricky to pinpoint from transport measurements. The electrical resistance of $CuInP_2S_6$ is shown in Fig. 3**a**. Although there is a significant decrease above 30 GPa, the slope of the resisitivity curve as well as the absolute value of ρ_{dc} are consistent with semiconducting behavior. According to our analysis [Fig. S8 Supplemental Information], the transport gap is several tens of meV at 46 GPa. Under these conditions, $CuInP_2S_6$ is still a weak metal at best. This is verified by (i) the beautiful red color of the crystal under these conditions along with (ii) the presence of unscreened phonons in the spectroscopic response [Fig. 3**b,c**]. To unambiguously distinguish semiconductor or bad metal behavior from true metallicity,[32] we measured the infrared reflectance as a function of pressure. In our hands, metallicity develops at approximately 63 GPa as evidenced by a Drude oscillator, which clearly screens the phonons in this system [Fig. 3**b,c**]. It is the disappearance of the phonons that is the true signature of metallicity.[32] We note that a 63 GPa insulator → metal transition is significantly higher than what was previously suggested in $CuInP_2S_6$[26] and also much larger than what is observed in the MPS_3 family of materials[3] - possibly due to the Cu site disorder.

Unraveling the space group sequence under pressure

We begin with the first critical pressure ($P_{C,1}$ = 4.6 GPa), which is a transition from monoclinic Cc to HP-I phase in $CuInP_2S_6$. The overall decrease in the number of phonons above $P_{C,1}$ suggests that HP-I is a new higher symmetry state. We employed the Bilbao crystallographic server as a tool to unravel the symmetry progression across $P_{C,1}$.[33–35] We used group-supergroup relations to determine potential space groups associated with the symmetry changes.[36–38] This approach provides several candidates for the HP-I phase in-

cluding $C2/c$, $Cmc2_1$, $Ccc2$, $Ama2$, $Aea2$, $Fdd2$, $P\bar{3}1m$, $P31c$, and $P\bar{3}1c$. Some of these space groups are well-recognized in the literature for this family of materials.[9,11,30] We also employed the COPL (Complete Order Parameter Listing) program of the Isotropy Software Suite to obtain a complete list of order parameters (irreducible representations) for the group-supergroup pairs, which helped to narrow down candidate space groups for the HP-I phase.[39] These candidates were further refined by examining the overall number of infrared- and Raman-active vibrational modes expected for each super-group and comparing the results with our spectral data. An example is shown in Fig. S3, Supplementary Information. The final candidates considered in this study are presented in Fig. 4**a**. An analysis of the energy landscape [Fig. 4**b**], demonstrates that $P31c$ has the lowest enthalpy in HP-I and is the superior match. Although we also considered an alternative $P31c$ configuration with six {112}-indexed spots in x-ray diffraction pattern in our calculations [Fig, S4, Supplementary Information], this structure was ruled out due to its significantly higher energy and dynamical instability compared to the $P31c$ phase presented here. A comparison of the frequency vs. pressure trends in the vicinity of $P_{C,1}$ is shown in Fig. 4**c,d**. We therefore assign $P_{C,1}$ as a structural phase transition from monoclinic $Cc \rightarrow$ trigonal $P31c$. This means that the monoclinic mirror plane perpendicular to the b lattice vector is replaced by a three-fold rotation axis along c, and glide planes are introduced to create a more isotropic axial structure. This is different than what is proposed in recent literature ($P\bar{3}1c$, and $P\bar{3}1m$),[9–11,15,30] but as discussed below, high pressure synchrotron x-ray measurements are consistent with the finding of a polar space group.

X-ray diffraction of a single crystal shows that HP-I phase hosts a unit cell with lattice constants $a = b = 5.9413(1)$ Å , $c = 12.029(8)$ Å , $\alpha = \beta = 90°$ and $\gamma = 120°$ at 4.9 GPa. Figure 5**a** shows the two-dimensional pattern at 6.1 GPa ($a = 5.925(2)$ Å, $c = 11.93(1)$ Å). The lattice parameters and our theoretical calculations are in good agreement [Table S3 Supplementary Information]. We have also plotted the experimental and theoretical lattice parameters and volume for both phases under hydrostatic pressure, which confirms that the volume decreases consistently with increasing pressure for each phase (Fig. S7, Supplementary Information). Most of the reflections clearly appear. All reflections are indexed to a trigonal or hexagonal unit cell [Fig. S6, Supplementary Information]. Indices are drawn separately to emphasize the symmetry of the various patterns, which fall in either the $\bar{3}m$ or $6/mmm$ Laue class.

Six bright reflections from the {112} and {114} families and five from the {222} family also appear due to the inherently large structure factor and possibly due to wrinkles in the sample surface. We consider all possible candidate structures for HP-I: $P6_3mc$, $P6_3/mmc$, $P6_322$, $P\bar{6}2c$, $P\bar{3}1m$, $P\bar{3}1c$, $P31c$, $P312$. $P6_3/mmc$ and $P6_322$ are immediately excluded because they are expected to have fewer than 15 infrared-active modes. $P6_3mc$ and $P\bar{6}2c$ host a set of predicted phonon mode energies that do not match with our infrared and Raman scattering results, so they are eliminated. $P\bar{3}1m$ was not considered because the atomic arrangement within a layer does not maintain that of the ambient phase. $P312$ and $P\bar{3}1c$ are excluded because they predict a three-fold reflection pattern from the {112} family, which we do not observe. We are once again left to consider $P31c$ as the most suitable space group for the HP-I phase. Figure 5**e** shows the HP-I structural model in which the sulfur atoms are nearly prismatically coordinated about the cations.

Next, we turn our attention to $P_{C,2}$ which is a structural phase transition from trigonal $P31c$ to a slightly different atomic arrangement in HP-II phase. It is evidenced by the appearance and disappearance of one phonon mode in the Raman scattering as well as the disappearance of one infrared-active mode in the absorbance - although it must be noted that these features are relatively small. We examined group-subgroup relationships for $P31c$ in the Bilbao crystallographic server.[28,33,36,37] The analysis provides a number of candidates for HP-II: $P1$, $P\bar{1}$, $P2_1$, Cc, $C2$, Pm, Cm, and $P3$. We also considered several space groups that have been observed in the literature[9,11,30] including $C2/c$, $P\bar{3}$, $P\bar{3}1c$, $P\bar{3}1m$, $P31c$, $P312$ and carried out lattice dynamics calculations to reveal their spectroscopic patterns. We can immediately see that the system does not revisit monoclinic Cc or $C2/c$, so we eliminate these from further consideration. After that, we employed the COPL program[39] which helped to omit $P\bar{1}$, $P2_1$, $P\bar{3}$, $P312$, and $P\bar{3}1c$. We are therefore left to select between $P1$, $P3$, and $P31c$. These candidates were refined by examining the overall number of infrared and Raman-active vibrational modes for each subgroup and comparing the results with our spectra. In addition, we compared first-principles lattice dynamics calculations for these subgroups with our experimental data. As shown in Fig. 4**c,d**, the $P31c$ space group offers a superior match for the HP-II phase as well, although some aspects of this $P31c$ phase are different due to sulfur rearrangement.

What does x-ray diffraction reveal about $P_{C,2}$? We find that HP-II is a trigonal phase

with lattice constants of $a = 5.802(2)$Å and $c = 10.05(1)$Å at 15 GPa [Fig. 5**b** and Fig. S6, Supplementary Information]. Remarkably, the reflections from the {112} family indicate a three-fold pattern. We thus consider trigonal structures, specifically those belonging to the $\bar{3}m$ Laue class: $P31c$, $P\bar{3}1c$, and $P312$. By integrating the pattern in 15° sectors about each {104} reflection [Fig. 5**d,e**], we see that the {104} reflections appearing near {112} suggest a three-fold intensity modulation. Such a feature is consistent only with the polar space groups, allowing us to exclude $P312$ and $P\bar{3}1c$ from further consideration. We are left to consider only $P31c$ as the structure of HP-II. There are, however, important differences compared with HP-I. The {112} intensities abruptly change the symmetry of their pattern across $P_{C,2}$, suggesting a rearrangement of S centers from nearly prismatic in HP-I to more octahedral in HP-II - an apparent restoration of symmetry in the sulfur sublattice [Fig. 5**c**].

The full symmetry progression of $CuInP_2S_6$ in this pressure window is thus $Cc \rightarrow P31c$ (prismatic sulfur) $\rightarrow P31c$ (octahedral sulfur). Importantly, all three space groups lack inversion symmetry and are polar - different from those reported previously.[9–11,15,30] Whether the high pressure phases are ferroelectric (switchable) or pyroelectric (not switchable) is not yet known. Both the calculated energy landscape and the pattern of vibrational modes support this sequence of events. Figure 4**b** displays the enthalpy as a function of pressure for several candidate space groups of $CuInP_2S_6$. Analysis of the energy landscape reveals a clear $Cc \rightarrow P31c$ crossover near 4.6 GPa. There is, however, no evidence for an energetically-preferred ground state above $P_{C,2} = 12$ GPa.

Evidence for copper migration in the Cc phase under pressure

It is well known that $CuInP_2S_6$ exhibits unconventional polarization switching behavior attributed to Cu^+ ion migration within the lamellae and across the van der Waals gap.[8,15,17,40–47] Prior works reveal a spontaneous polarization of 4.07 μC/cm^2 that increases to 6.05 μC/cm^2 at 0.5 GPa, starts to decrease near 1.4 GPa, and vanishes above 3 GPa.[10,11] A similar trend is observed in the second harmonic generation, although the signal reaches a maximum at 3.4 GPa and is not quenched until crossing $P_{C,1}$. Despite the slight differences in these measurements, both long and short length and time scale techniques demonstrate that polarization increases with pressure - at least in a certain range. Unfortunately, even the closest examina-

tion of our frequency vs. pressure data [Fig. 2**b,f**] yields very little except an exceptionally clear $Cc \rightarrow P31c$ structural phase transition at $P_{C,1} = 4.6$ GPa. A deeper analysis is required to reveal evidence for anomalous changes in polarization within the Cc phase and to resolve these controversies. To perform a detailed analysis of Cu ion migration in the Cc phase, we bring together Raman scattering spectroscopy and x-ray diffraction with diamond anvil cell techniques and complementary theoretical Berry phase calculations[48,49].

Figure 6**a** shows a close-up view of the Raman scattering response in the Cc phase. In addition to intensity changes, the phonon linewidths broaden significantly between 0.5 and 2.5 GPa, indicating reduced phonon lifetimes. Since the phonon lifetime $\tau_{ph} = \hbar/\gamma$, an increase in the linewidth (γ) yields a shorter phonon lifetime.[50–52] For example, the A″ mode at 69 cm^{-1} exhibits a lifetime of 0.84 ps under ambient conditions, which decreases to 0.49 ps as the linewidth broadens to its maximum at 1.96 GPa. Similar results were reported by Rao *et al.* but not considered further.[7] Since the effects are especially pronounced in the out-of-plane phonon modes, we attribute the pressure-induced decrease in the phonon lifetimes to changes (and disorder) in the Cu^+ position. We speculate that the overall randomness in the Cu^+ position due to migration shortens the phonon lifetimes in this pressure region. The curious aspect is how this randomization process is connected with an increase in polarization.

To gain further insight into the relation between the movement of Cu^+ ions with polarization, we investigated the polarization component along the out-of-plane direction (c-axis) using the Berry phase approach[48,49] under hydrostatic pressure ranging from 0 to 40 GPa [Fig. 6**b**]. At ambient pressure, where the monoclinic Cc phase is stable, $CuInP_2S_6$ exhibits a low polarization state, with a value of 4.08 $\mu C/cm^2$. Above 0.6 GPa, the Cu^+ ions shift into a different configuration, following the increasing experimental and theoretical trend,[11,15,24,53] and polarization increases to 11.33 $\mu C/cm^2$. This increase corresponds to the movement of Cu^+ ions from within the S-centered octahedral plane to an out-of-plane position. Above approximately 1.5 GPa, the Cu^+ ion tends to migrate toward the interlayer S atoms. As shown by our enthalpy calculations [Fig. 4**b**], this migration is accompanied by a reduction in polarization, indicating a transition from the Cc phase to the $P31c$ phase near 4.6 GPa. This structural change reduces the polarization - a trend that is supported by the x-ray diffraction results discussed below.

Figure 6**c** displays the powder x-ray diffraction of $CuInP_2S_6$ which contains a number of $(00l)$ reflections that are sensitive to the occupancies and positions of the two copper sites at ambient pressure. Our simulation of the powder diffraction reveals that the (004)/(002) ratio should depend explicitly upon the Cu position [Fig. 6**d**]. The shaded region between the two outer pink curves marks the ratios expected from equal tiny displacements of the two Cu^+ positions normal to the S-plane in the Cc structure. The ratio deviates markedly from this range when (i) Cu^+ migrates to the center of the slab (●) and (ii) atoms rearrange into a $C2/c$ structure (★, ⧫). Although the exact site occupancies of Cu are not determined, the measured intensity ratios indicate that pressure modifies these occupancies and slightly displaces the Cu^+ ions toward the van der Waals gap. However, we find no evidence for a complete transition to the $C2/c$ phase or for Cu^+ migration to the center of the slab in the low-pressure regime, which confirms that $CuInP_2S_6$ is in the monoclinic Cc phase. These observations align with our enthalpy calculations, which suggest that such transformations are energetically unfavorable at low pressure.

To gain additional insight, we conducted a single-crystal x-ray diffraction measurement. Faint streaks develop alongside the characteristic reflections at 0.2 GPa [Fig. S6, Supplementary Information]. The streaks reconfigure near 1.5 GPa. Additional $(hkl, l \neq 0)$ reflections from the Cc phase emerge, new peaks consistent with a trigonal phase appear, and the Cc reflections broaden into diffuse arcs - coinciding with the onset of remanent polarization decay[10] and persist up to $P_{C,1}$. The evolution of these streaks suggests migration and rearrangement of clustered defects, such as Cu vacancies, displaced S or P atoms, and local layer distortions. Minor diffusion of $In_{4/3}P_2S_6$ is also possible.[7,8] The migration of these defects could facilitate nanoscale sliding, promoting local transitions into a trigonal structure, which is less polar [Fig. 6**b**], even though the $CuInP_2S_6$ maintains a monoclinic Cc phase overall. Furthermore, the emergence of $(hkl, l \neq 0)$ reflections suggests out-of-plane buckling, wrinkling, or fracturing during defect migration. These effects could reduce the remanent polarization of the entire sample. Polarization enhancement through "pressure aging" supports this picture, indicating the presence of "trapped" or metastable states[54] that further enrich the P–T phase diagram of this system.

METHODS

Crystal growth and diamond anvil cell loading: High-quality single crystals of $CuInP_2S_6$ were prepared by chemical vapor transport techniques as described previously.[8] Care was taken to ascertain the correct phase. To study high-pressure states, we loaded a small piece of *ab*-plane oriented single crystal (approximately 70 μm in size) into a symmetric diamond anvil cell from Jade Corporation. The cell has type 2as diamonds with 400 µm culets. We employed a pre-indented stainless steel gasket with a thickness of 80 μm; the hole size was 100 μm. Along with the sample, a pressure medium and an annealed ruby ball were also loaded into the gasket. Depending on the measurement, either KBr (Raman and middle infrared) or petroleum jelly (far infrared) was used as the pressure medium. A proper pressure-transmitting medium ensures that the sample experiences quasi-hydrostatic conditions as pressure is increased. Ruby fluorescence was used for pressure determination.[55,56] The overall shape of ruby fluorescence confirms quasi-hydrostatic conditions [Fig. S1, Supplementary information].

Spectroscopic measurements: Synchrotron-based infrared measurements were performed using facilities of the 22-IR-1 beamline at the National Synchrotron Light Source II at Brookhaven National Laboratory. High pressure infrared measurements were carried out in both transmittance and reflectance mode over the far and middle infrared frequency range (50 - 8000 cm^{-1}) with a resolution of 2 or 4 cm^{-1}, respectively. The synchrotron source and helium-cooled bolometer were used in the far infrared, whereas a globar source and nitrogen-cooled MCT detector were employed for middle infrared work. Depending on whether far or middle infrared spectroscopy was of interest, we used either petroleum jelly or KBr as a pressure-transmitting medium. Raman scattering measurements were performed in the back-scattering geometry using a Horiba LabRAM HR Evolution Raman spectrometer. The instrument employs a 532 nm excitation wavelength, a power of 0.15 mW, a 1800 line/mm grating, and a liquid nitrogen-cooled CCD detector. We focused on the 0 - 750 cm^{-1} frequency range. To enhance the signal-to-noise ratio, we integrated for 30 seconds and averaged three times. Both the infrared absorbance and Raman scattering response of $CuInP_2S_6$ were the same after pressure cycling [Fig. S2, Supplementary information].

Symmetry analysis: We performed a group - subgroup analysis with the support of the Bilbao crystallographic server.[33–35] In order to predict super- and sub-groups, we analyzed the appearance and disappearance of various phonons which allows us to move up and down the symmetry tree according to a logical symmetry progression. At the same time, we tested a number of additional space groups that have been sighted in related van der Waals solids. Candidates were tested by calculating their energies relative to other structures under appropriate pressure condition, relaxing the structure to one with a suitable match to the experiments. In each case, we compared the predicted lattice dynamics of that candidate structure to our measured results.

X-ray diffraction: We conducted single-crystal and powder x-ray diffraction measurements at BL10XU/SPring-8 at room temperature using a diamond anvil cell. We used Si-oil as a pressure transmitting medium and employed ruby-florescence method for pressure measurement.[55] The wavelength of all measurement is 0.6240 Å (19.87 keV). The sample was rotated $\pm 10^{\circ}$ during the measurement. The single crystal was exfoliated from a larger single crystal and cut to the size of a sample chamber (100 μm in diameter, 60 μm in thickness) on a gasket (SUS310) in a diamond anvil cell. Powder sample was prepared by crushing a single crystal using a sharp knife blade. To avoid inducing strain or distortion in the crystals, we did not use a mortar and pestle. We collected the x-ray diffraction with an imaging plate (RIGAKU R-AXIS IV++, 300 × 300 mm^2, pixel size: 0.10 × 0.10 mm^2).

Electrical transport: We measured the electrical resistance of a $CuInP_2S_6$ single crystal under pressure. The single-crystal sample is confined in a diamond anvil cell with tiny ruby chips and the electrical probes made of thin platinum (Pt) wires. The gasket was insulated by coating a stainless steel gasket with a compressed mixture of diamond powder and epoxy resin. A plate of NaCl is placed beneath the sample to serve as a pressure medium, thereby making the pressure distribution across the sample as uniform as possible. The detailed configuration can be found in Ref. 57. The pressure was tuned at room temperature. The electrical resistance vs. temperature curve was obtained by changing the temperature between 100 and 300 K in a closed-cycle cryostat.

First-principles calculations: All first-principles density functional theory (DFT) calculations were performed using the Vienna *ab initio* Simulation Package (VASP),[58,59] employing the generalized gradient approximation (GGA)[60] as parameterized by Perdew-

Burke-Ernzerhof for solids (PBEsol).[61] The number of valence electrons in the GGA pseudopotentials used were 11 ($3d^{10}4s^1$), 3 ($5s^25p^1$), 5 ($3s^23p^3$), and 6 ($3s^23p^4$) for Cu, In, P, and S atoms, respectively. A plane-wave energy cutoff of 600 eV was adopted for all DFT calculations. The structures were optimized until the residual Hellmann–Feynman forces on each atom were less than 0.001 eV/Å, with a total self-consistent energy convergence of 10^{-7} eV. The DFT-D3 method was incorporated to account for weak van der Waals interactions, ensuring accurate potential energy and interatomic force corrections.[62,63] The Brillouin zone was sampled using a Γ-centered **k**-point mesh of size $8 \times 8 \times 4$. The PHONOPY package was employed to calculate the zone-center phonon frequencies and phonon eigenvectors of the DFT-optimized structures at 0 K using the finite-displacement approach.[64] The Bilbao crystallographic server was used to analyze the symmetry of the phonon modes.[35] The theoretical infrared spectra were computed by evaluating the mode dynamical charges associated with each infrared-active phonon eigendisplacement. The theoretical Raman spectra were simulated by averaging the Raman activity tensor corresponding to each Raman-active phonon eigenmode at the Γ-point.

DATA AVAILABILITY

The authors declare that the data supporting the findings of this study are available within the paper and its Supplementary Information files. All raw data generated in this study are provided in the Source Data file. Source data are provided with this paper.

CODE AVAILABILITY

The authors declare that the codes supporting the findings of this study are available within the paper and its Supplementary Information files. All raw data generated in this study are provided in the Source Data file. Source data are provided with this paper.

ACKNOWLEDGEMENTS

JLM thanks the Physical Behavior of Materials, Basic Energy Sciences, U.S. Department of Energy (Contract number DE-SC0023144) for support of this work. SS acknowledges sup-

port from the U.S. Department of Energy, Office of Science, Office of Fusion Energy Sciences, Quantum Information Science program under Award No. DE-SC-0020340. TM is supported by the Air Force Office of Scientific Research under award number FA2386-23-1-4112 and the NIP research contract (2024-25). The authors also thank the Pittsburgh Supercomputer Center (Bridges2) funded by the Advanced Cyberinfrastructure Coordination Ecosystem: Services & Support (ACCESS) program, which is supported by National Science Foundation Grants No. 2138259, No. 2138286, No. 2138307, No. 2137603, and No. 2138296. SWC is funded by the W. M. Keck Foundation grant to the Keck Center for Quantum Magnetism at Rutgers University. MAS thanks the Air Force Office of Scientific Research (AFOSR) Grant No. LRIR 23RXCOR003 and AOARD-NSTC Grant No. F4GGA21207H002. Work at the National Synchrotron Light Source II at Brookhaven National Laboratory is funded by the Department of Energy (DE-AC98-06CH10886). Use of the 22-IR-1 beamline is supported by the National Science Foundation Division of Earth Sciences (EAR) SEES: Synchrotron Earth and Environmental Science (EAR-2223273) and Chicago/DOE Alliance Center (CDAC) DENA-0004153. The experiments at BL10XU beamline in SPring-8 are conducted under the awarded machine times No.2024A1382, No.2024B1285, and No.2025A1251. We thank Rahul Rao for useful discussions related to the inception of this study.

AUTHOR CONTRIBUTIONS

TM, SS, and JLM designed the study. SWC, RS and MAS grew the crystals. SS, BT, ZL, and JLM performed the high pressure spectroscopic measurements. SS, LL, YG, and KAS analyzed the spectral data with the guidelines of JLM. SS and PM performed complementary first-principles calculations and discussed the results with SS, BT, and JLM. BGS, HK, TM, and RVS conducted x-ray diffraction and analyzed the data. SS, PM, BGS, SS, TM, and JLM designed the figures and wrote the manuscript. All authors read and commented on the text.

COMPETING INTERESTS

The authors declare no competing financial or non-financial interests.

[1] Grochala, W., Hoffmann, R., Feng, J. & Ashcroft, N. W. The chemical imagination at work in very tight places. *Angew. Chem* **46**, 3620–3642 (2007).

[2] Mao, H.-K., Chen, X.-J., Ding, Y., Li, B. & Wang, L. Solids, liquids, and gases under high pressure. *Rev. Mod. Phys* **90**, 015007 (2018).

[3] Matsuoka, T., Kim, H.-S., Samanta, S., Musfeldt, J. L. & Mandrus, D. G. MPX_3 van der Waals magnets under pressure (M = Mn, Ni, V, Fe, Co, Cd; X= S, Se). *Front. Mater* **11**, 1362744 (2024).

[4] Aoyama, T. *et al.* Giant spin-driven ferroelectric polarization in $TbMnO_3$ under high pressure. *Nat. Commun* **5**, 4927 (2014).

[5] Guranich, P. *et al.* Influence of hydrostatic pressure on the dielectric properties of $CuInP_2S_6$ and $CuInP_2Se_6$ layered crystals. In *J. Phys. Conf. Ser*, vol. 79, 012009 (IOP Publishing, 2007).

[6] Susner, M. A., Chyasnavichyus, M., McGuire, M. A., Ganesh, P. & Maksymovych, P. Metal thio-and selenophosphates as multifunctional van der Waals layered materials. *Adv. Mater.* **29**, 1602852 (2017).

[7] Rao, R., Conner, B. S., Selhorst, R. & Susner, M. A. Pressure-driven phase transformations and phase segregation in ferrielectric $CuInP_2S_6$-$In_{4/3}P_2S_6$ self-assembled heterostructures. *Phys. Rev. B* **104**, 235421 (2021).

[8] Neal, S. N. *et al.* Vibrational properties of $CuInP_2S_6$ across the ferroelectric transition. *Phys. Rev. B* **105**, 075151 (2022).

[9] Bu, K. *et al.* Enhanced second-harmonic generation of van der Waals $CuInP_2S_6$ via pressure-regulated cationic displacement. *Chem. Mater* **35**, 242–250 (2022).

[10] Yao, X. *et al.* Anomalous polarization enhancement in a van der Waals ferroelectric material under pressure. *Nat. Commun* **14**, 4301 (2023).

[11] Zhou, Z. *et al.* Sliding-mediated ferroelectric phase transition in $CuInP_2S_6$ under pressure. *Appl. Phys. Rev* **11** (2024).

[12] Liu, F. *et al.* Room-temperature ferroelectricity in $CuInP_2S_6$ ultrathin flakes. *Nat. Commun* **7**, 1–6 (2016).

[13] Morozovska, A. N., Eliseev, E. A., Kalinin, S. V., Vysochanskii, Y. M. & Maksymovych, P. Stress-induced phase transitions in nanoscale $CuInP_2S_6$. *Phys. Rev. B* **104**, 054102 (2021).

[14] Zhou, Z. *et al.* Unconventional polarization fatigue in van der waals layered ferroelectric ionic conductor $CuInP_2S_6$. *Nat. Commun* **14**, 8254 (2023).

[15] Brehm, J. A. *et al.* Tunable quadruple-well ferroelectric van der Waals crystals. *Nat. Mater.* **19**, 43–48 (2020).

[16] Neumayer, S., Qiao, H. & Balke, N. Competing polar phases in 2D ferroelectric transition metal thio-and selenophosphates. *Appl. Phys. Lett* **126** (2025).

[17] Seleznev, D., Singh, S., Bonini, J., Rabe, K. M. & Vanderbilt, D. Cyclic ferroelectric switching and quantized charge transport in $CuInP_2S_6$. *Phys. Rev. B* **108**, L180101 (2023).

[18] Liang, L. *et al.* Configurable kinetics of polarization switching via ion migration in ferroionic $CuInP_2S_6$. *Nat. Commun* **16**, 4462 (2025).

[19] Li, T. *et al.* Realization of sextuple polarization states and interstate switching in antiferroelectric $CuInP_2S_6$. *Nat. Commun* **15**, 2653 (2024).

[20] Reimers, J. R., Tawfik, S. A. & Ford, M. J. van der Waals forces control ferroelectric–antiferroelectric ordering in $CuInP_2S_6$ and $CuBiP_2Se_6$ laminar materials. *Chem. Sci* **9**, 7620–7627 (2018).

[21] Ma, R.-R. *et al.* Nanoscale mapping of Cu-ion transport in van der Waals layered $CuCrP_2S_6$. *Adv. Mater. Interfaces* **9**, 2101769 (2022).

[22] Dushaq, G., Serunjogi, S., Tamalampudi, S. R. & Rasras, M. Electro-optic tuning in composite silicon photonics based on ferroionic 2D materials. *Light Sci. Appl.* **13**, 92 (2024).

[23] Cho, K. *et al.* Tunable ferroelectricity in van der Waals layered antiferroelectric $CuCrP_2S_6$. *Adv. Funct. Mater* **32**, 2204214 (2022).

[24] Mohammadi, P. & Singh, S. Pressure-induced phase transitions and asynchronous ferroelectric switching mechanism in $CuInP_2S_6$. *Phys. Rev. B* **112**, 125205 (2025).

[25] Grzechnik, A., Cajipe, V., Payen, C. & McMillan, P. Pressure-induced phase transition in ferrielectric $CuInP_2S_6$. *Solid State Commun* **108**, 43–47 (1998).

[26] Rao, R., Conner, B. S., Jiang, J., Pachter, R. & Susner, M. A. Raman spectroscopy study of pressure-induced phase transitions in single crystal $CuInP_2S_6$. *J. Chem. Phys* **159** (2023).

[27] Kong, L. & Liu, G. Synchrotron-based infrared microspectroscopy under high pressure: An introduction. *Matter Radiat. Extrem.* **6** (2021).

[28] Harms, N. C. *et al.* Symmetry progression and possible polar metallicity in $NiPS_3$ under pressure. *npj 2D Mater. Appl.* **6**, 40 (2022).

[29] Harms, N. C. *et al.* Piezochromism in the magnetic chalcogenide $MnPS_3$. *npj Quantum Mater* **5**, 56 (2020).

[30] Fang, S. *et al.* Significant enhancement of optoelectronic properties in $CuInP_2S_6$ via pressure-induced structural phase transition. *J. Phys. Chem. C* **127**, 8383–8388 (2023).

[31] Shah, S. *et al.* Symmetry progression and band vs. Mott character of $CdPS_3$ under pressure. *APL Mater.* **13**, 071127 (2025).

[32] Okamura, H. *et al.* Pressure suppression of unconventional charge-density-wave state in $PrRu_4P_{12}$ studied by optical conductivity. *Phys. Rev. B* **85**, 205116 (2012).

[33] Ivantchev, S., Kroumova, E., Madariaga, G., Pérez-Mato, J. & Aroyo, M. Subgroupgraph: a computer program for analysis of group–subgroup relations between space groups. *J. Appl. Crystallogr* **33**, 1190–1191 (2000).

[34] Aroyo, M. I. *et al.* Crystallography online: Bilbao crystallographic server. *Bulg. Chem. Commun.* **43**, 183–197 (2011).

[35] Kroumova, E. *et al.* Bilbao crystallographic server: useful databases and tools for phase-transition studies. *Ph. Transit.* **76**, 155–170 (2003).

[36] Kitaev, Y. E., Panfilov, A., Tasci, E. & Aroyo, M. High-symmetry phase prediction using trees of group–supergroup relations. *Phys. Solid State* **57**, 2297–2304 (2015).

[37] Zúñiga, F. J., Perez-Mato, J. M., Orobengoa, D., Petricek, V. & Breczewski, T. Symmetry mode analysis of the phase transitions in Rb_2ZnBr_4. *Z. Kristallogr* **226**, 454–466 (2011).

[38] Langston, L. J. *et al.* Pressure-induced structural phase transitions in CrSBr. *npj Quantum Mater* **10**, 1–8 (2025).

[39] Stokes, H. T., Hatch, D. M. & Campbell, B. J. Isodistort, isotropy software suite. *Iso. Byu. Edu* (2022).

[40] Neumayer, S. M. *et al.* Alignment of polarization against an electric field in van der Waals ferroelectrics. *Phys. Rev. Appl* **13**, 064063 (2020).

[41] Zhou, S. *et al.* Anomalous polarization switching and permanent retention in a ferroelectric ionic conductor. *Mater. Horiz.* **7**, 263–274 (2020).

[42] Jiang, X. *et al.* Dual-role ion dynamics in ferroionic $CuInP_2S_6$: revealing the transition from ferroelectric to ionic switching mechanisms. *Nat. Commun* **15**, 10822 (2024).

[43] Morozovska, A. N. *et al.* Ferri-ionic coupling in $CuInP_2S_6$ nanoflakes: Polarization states and controllable negative capacitance. *Phys. Rev. Appl* **22**, 034059 (2024).

[44] Zhang, D. *et al.* Anisotropic ion migration and electronic conduction in van der Waals ferroelectric $CuInP_2S_6$. *Nano Lett* **21**, 995–1002 (2021).

[45] Neumayer, S. M. *et al.* Giant negative electrostriction and dielectric tunability in a van der Waals layered ferroelectric. *Phys. Rev. Mater.* **3**, 024401 (2019).

[46] Balke, N. *et al.* Locally controlled Cu-ion transport in layered ferroelectric $CuInP_2S_6$. *ACS Appl. Mater. Interfaces* **10**, 27188–27194 (2018).

[47] Neumayer, S. M. *et al.* The concept of negative capacitance in ionically conductive van der Waals ferroelectrics. *Adv. Energy Mater.* **10**, 2001726 (2020).

[48] Vanderbilt, D. *Berry Phases in Electronic Structure Theory: Electric Polarization, Orbital Magnetization and Topological Insulators* (Cambridge University Press, Cambridge, 2018).

[49] Resta, R. & Vanderbilt, D. Theory of Polarization: A Modern Approach. In *Physics of Ferroelectrics: A Modern Perspective*, 31–68 (Springer, Berlin, Heidelberg, 2007).

[50] Sun, Q.-C. *et al.* Spectroscopic determination of phonon lifetimes in rhenium-doped MoS_3 nanoparticles. *Nano Lett* **13**, 2803–2808 (2013).

[51] Gu, Y. *et al.* Phonon mixing in the charge density wave state of ScV_6Sn_6. *npj Quantum Mater* **8**, 58 (2023).

[52] Lory, P.-F. *et al.* Direct measurement of individual phonon lifetimes in the clathrate compound $Ba_{7.81}Ge_{40.67}Au_{5.33}$. *Nat. Commun* **8**, 491 (2017).

[53] Zhang, D., Schoenherr, P., Sharma, P. & Seidel, J. Ferroelectric order in van der Waals layered materials. *Nat. Rev. Mater* **8**, 25–40 (2023).

[54] Luo, H. *et al.* Pressure aging: An effective process to liberate the power of high-pressure materials research. *Proc. Natl. Acad. Sci. U.S.A.* **121**, e2416835121 (2024).

[55] Mao, H., Xu, J.-A. & Bell, P. Calibration of the ruby pressure gauge to 800 kbar under quasi-hydrostatic conditions. *J. Geophys. Res.: Solid Earth* **91**, 4673–4676 (1986).

[56] Xu, J., Mao, H. & Bell, P. High-pressure ruby and diamond fluorescence: observations at 0.21 to 0.55 terapascal. *Science* **232**, 1404–1406 (1986).

[57] Matsuoka, T. *et al.* Pressure-induced insulator-to-metal transition in the van der Waals compound $CoPS_3$. *Phys. Rev. B* **107**, 165125 (2023).

[58] Kresse, G. & Furthmüller, J. Efficient iterative schemes for ab initio total-energy calculations using a plane-wave basis set. *Phys. Rev. B* **54**, 11169 (1996).

[59] Kresse, G. & Furthmüller, J. Efficiency of ab-initio total energy calculations for metals and semiconductors using a plane-wave basis set. *Comput. Mater. Sci* **6**, 15–50 (1996).

[60] White, J. & Bird, D. Implementation of gradient-corrected exchange-correlation potentials in Car-Parrinello total-energy calculations. *Phys. Rev. B* **50**, 4954 (1994).

[61] Perdew, J. P. *et al.* Restoring the Density-Gradient Expansion for Exchange in Solids and Surfaces. *Phys. Rev. Lett* **100**, 136406 (2008).

[62] Grimme, S., Antony, J., Ehrlich, S. & Krieg, H. A consistent and accurate ab initio parametrization of density functional dispersion correction (DFT-D) for the 94 elements H-Pu. *J. Chem. Phys* **132** (2010).

[63] Grimme, S., Ehrlich, S. & Goerigk, L. Effect of the damping function in dispersion corrected density functional theory. *J. Comput. Chem* **32**, 1456–1465 (2011).

[64] Togo, A. & Tanaka, I. First principles phonon calculations in materials science. *Scr. Mater* **108**, 1–5 (2015).

[65] Maisonneuve, V., Evain, M., Payen, C., Cajipe, V. & Molinie, P. Room-temperature crystal structure of the layered phase $Cu^{I}In^{III}P_2S_6$. *J. Alloys Compd* **218**, 157–164 (1995).

[66] Momma, K. & Izumi, F. VESTA 3 for three-dimensional visualization of crystal, volumetric and morphology data. *J. Appl. Crystallogr* **44**, 1272–1276 (2011).

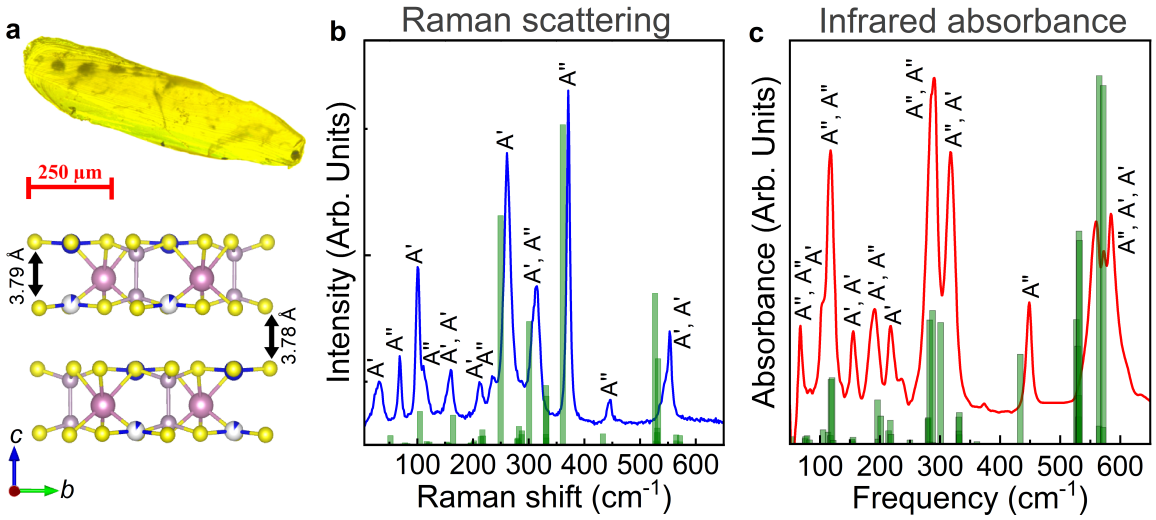

FIG. 1. **Crystal structure and vibrational properties of $CuInP_2S_6$. a** Photo of a *ab*-plane single crystal and rendering of the *Cc* crystal structure[65] where Cu, In, P, and S are indicated using blue-white, purple, gray, and yellow spheres visualized using VESTA software.[66] The sheet thickness and van der Waals gap are indicated. **b,c** Raman scattering response and infrared absorbance of $CuInP_2S_6$ at ambient conditions along with the theoretically predicted spectrum for the *Cc* space group (green lines). Mode symmetries are labeled.

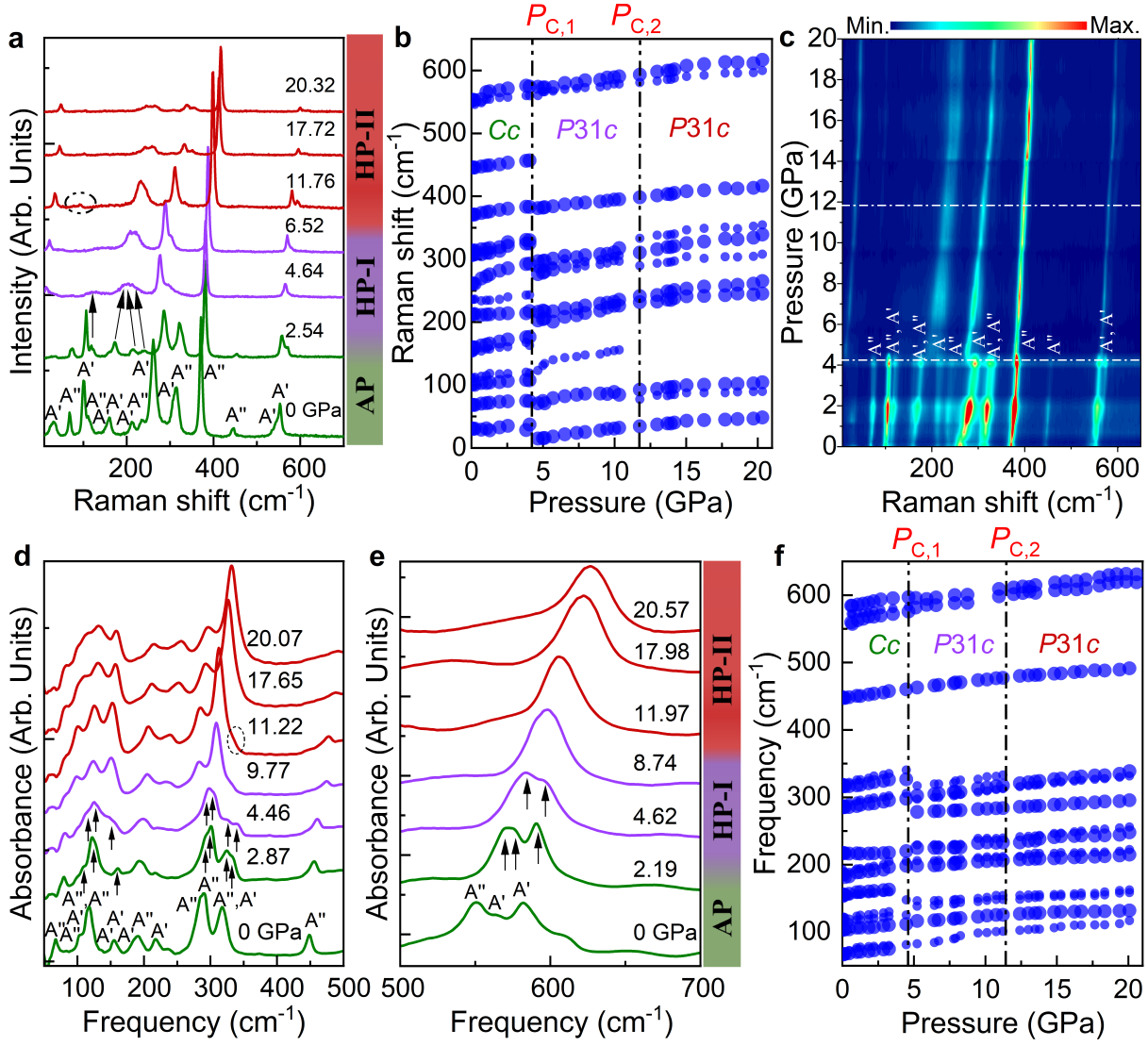

FIG. 2. **Vibrational properties of $CuInP_2S_6$ as a function of pressure.** **a** Raman scattering response under compression at room temperature. Mode symmetries are labeled. **b** Frequency vs. pressure plot of these data. **c** Contour plot of the Raman scattering intensity as a function of pressure. Critical pressures near 4.6 and 12 GPa are indicated by dashed horizontal lines. **d,e** Infrared absorbance of $CuInP_2S_6$ under compression at 300 K. **f** Frequency vs. pressure plot of these data. The black dashed lines denote critical pressures, and the arrows and circles indicate features of interest. Spectra in the *Cc* space group are shown in green, whereas those in the high pressure phases are in purple (HP-I) and red (HP-II). Phonon intensity is indicated by the size of the blue circles in the frequency vs. pressure plots. The vibrational properties of $CuInP_2S_6$ are fully reversible upon decompression [Fig. S2, Supplementary Information].

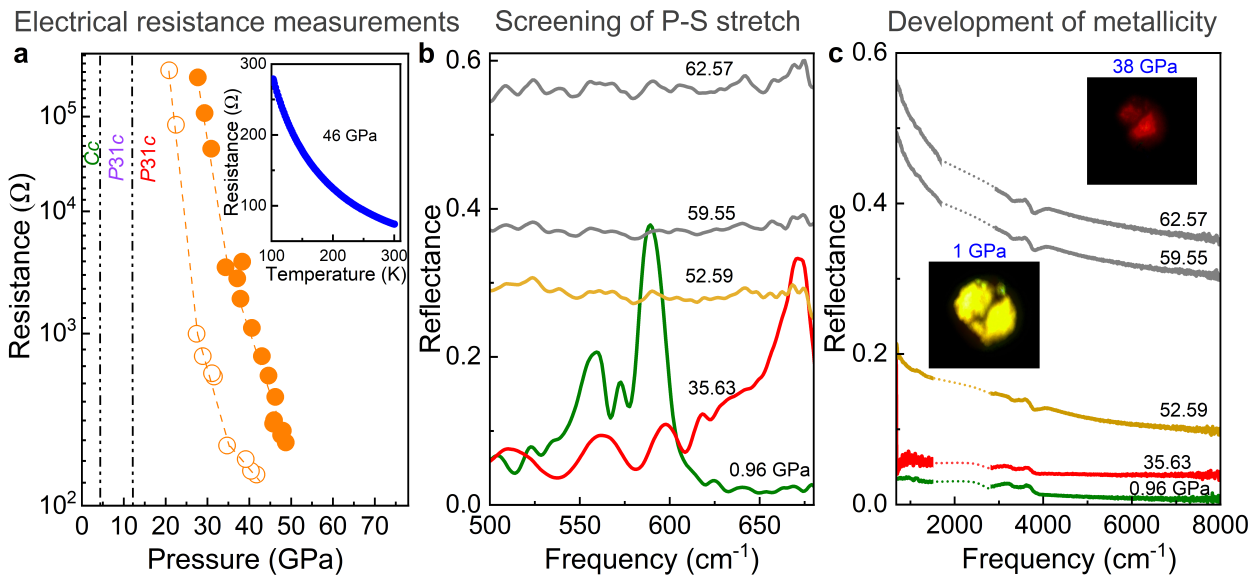

FIG. 3. **Insulator-to-metal transition in $CuInP_2S_6$ near 63 GPa.** **a** Electrical resistance vs. pressure at room temperature, where the filled and empty spheres represent the data recorded during compression and decompression measurements, respectively. Vertical lines separate the different structural phases which are indicated. Inset: resistance vs. temperature at 46 GPa from which we estimate an activation energy of approximately 29 meV. **b,c** Reflectance as a function of pressure showing how the phonons shift and become screened as metallicity develops. The photos in **c** show the sample at 1 and 38 GPa with exposure times of 1 and 704 ms, respectively. Dashed lines omit the well-known diamond signatures and guide the eye.

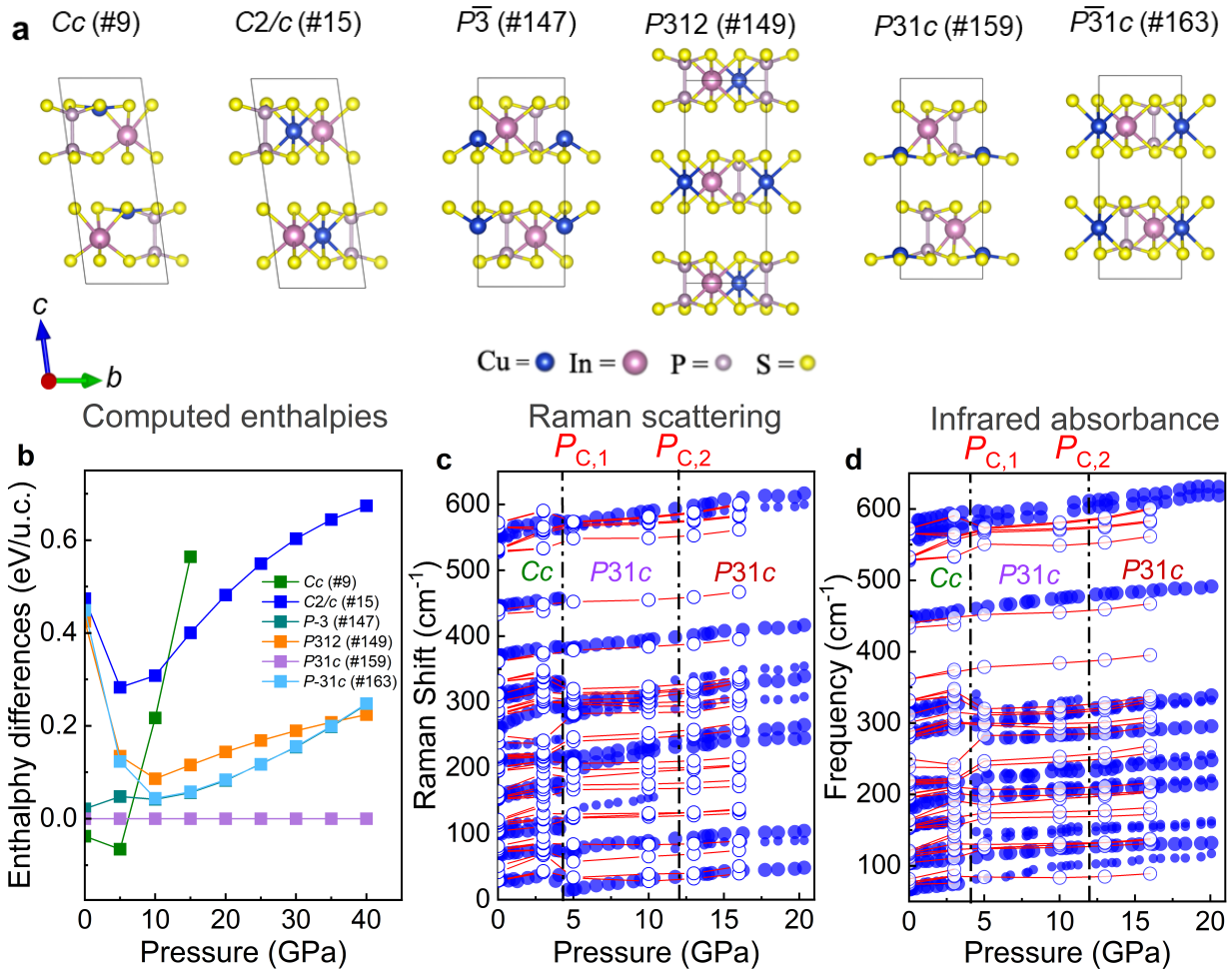

FIG. 4. **Candidate structures, energy landscape, and frequency trends under pressure.** **a** Computed candidate space groups for high pressure in $CuInP_2S_6$. **b** Computed enthalpies of these space groups as a function of pressure. **c,d** Frequency vs. pressure comparison of theoretical (blue filled) and experimental (red empty) modes for both Raman scattering and infrared absorbance. The theoretical frequencies are shifted by ≈ 9 cm^{-1}. The black dashed lines denote critical pressures.

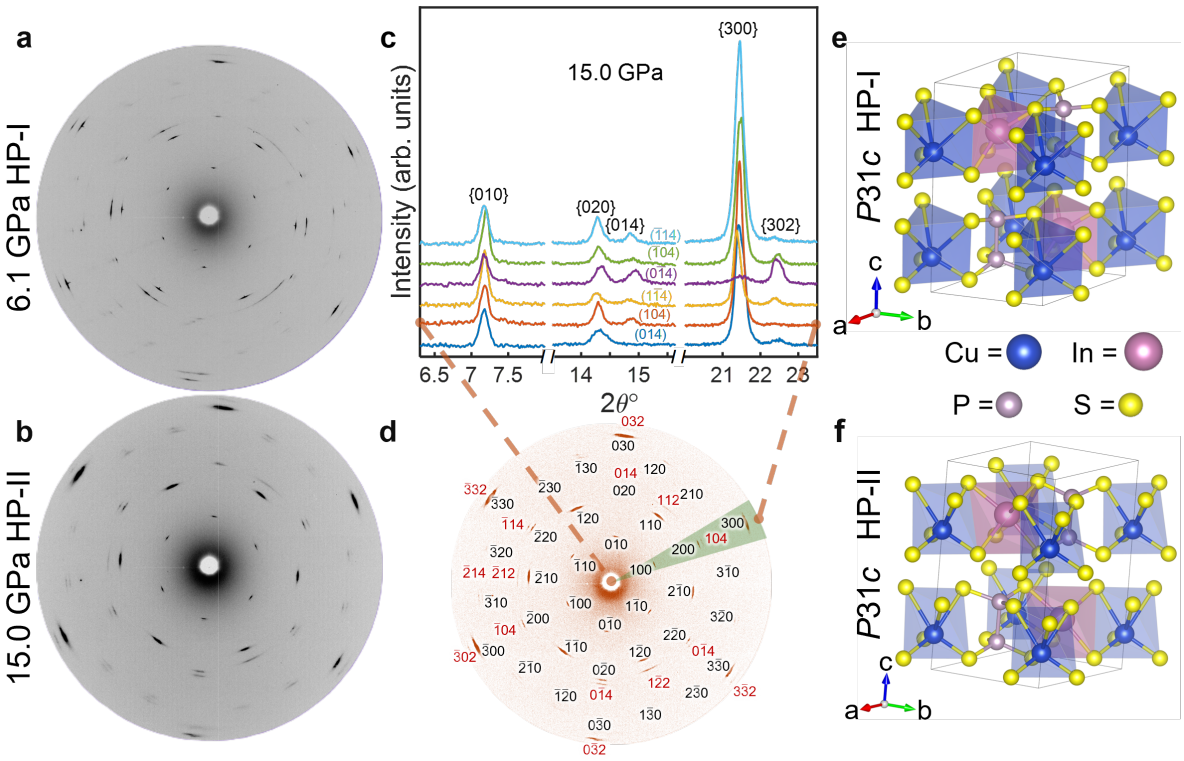

FIG. 5. **X-ray diffraction measurements of single crystal $CuInP_2S_6$. a,b** 2D x-ray diffraction patterns at pressures representing the HP-I and HP-II. **c** Integrated profiles from each of the six sectors about reflections from the {104} family shown below. **d** Indexed x-ray diffraction pattern in HP-II (at 15.0 GPa) superimposed with one 15°-wide sector (green). The arrangement of indices also holds for HP-I. Reflections from $l \neq 0$ are in red fonts. **e,f** Suggested structures from x-ray diffraction analysis.

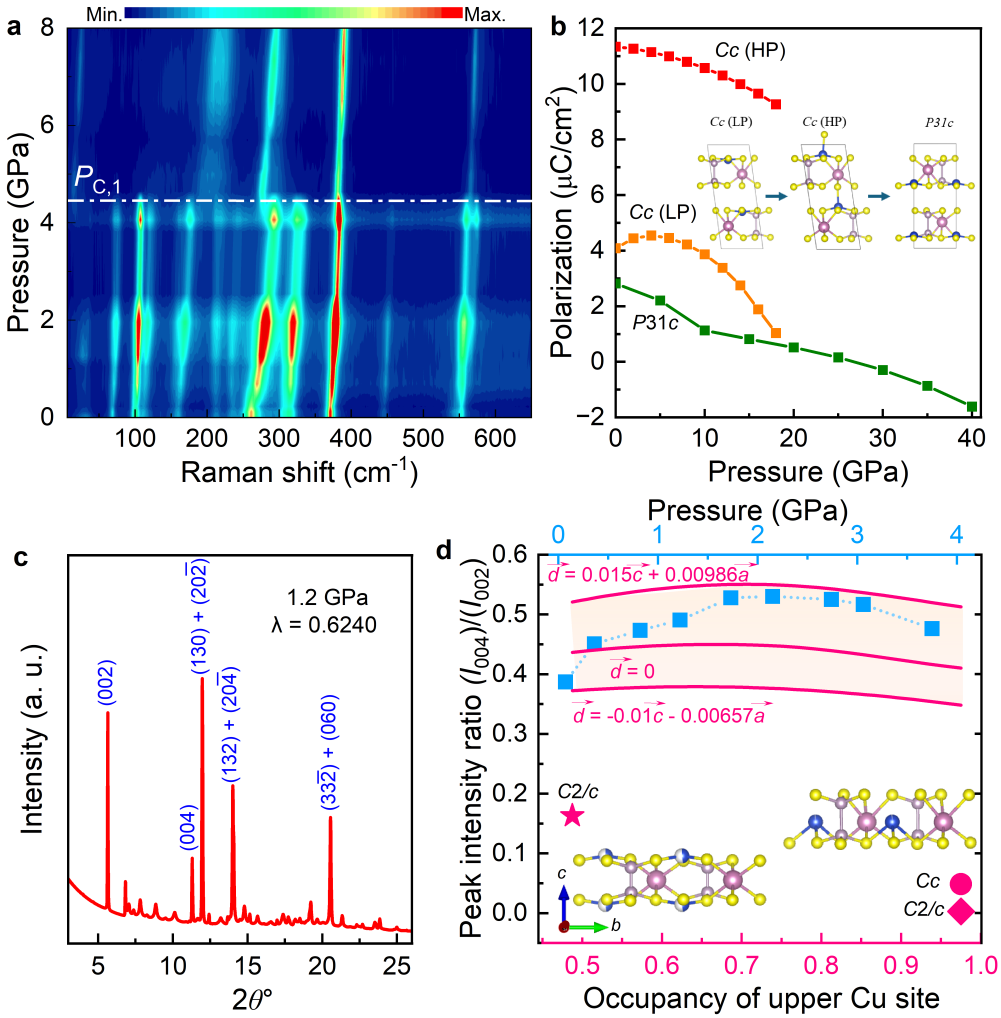

FIG. 6. **Evidence for Cu movement in the** Cc **phase. a** Close-up view of the Raman scattering response of $CuInP_2S_6$ in the vicinity of $P_{C,1}$ in the form of a contour plot, where we find a linewidth and intensity changes within the Cc phase. The significant linewidth broadening between 0.5 and 2.5 GPa is consistent with increasing polarization.[9–11] **b** Calculated ferroelectric polarization in the c direction for Cc (low polarization (LP) and high polarization (HP) state) and $P31c$ phases under pressure. **c** Powder x-ray diffraction pattern at 1.2 GPa. **d** Measured intensity ratios of the (004) to (002) peaks from powder X-ray diffraction profiles at various pressures (top x-axis, pale blue squares). Pink solid curves and filled symbols, ★, ⧫, and ● are simulated ratios vs. occupancy of the upper copper site (bottom x-axis) using ambient phase lattice parameters.[65] The two copper sites maintain a total occupancy of 0.975. Vectors $\vec{d}$ corresponding to each curve are displacements of Cu^+ centers starting at ambient pressure positions ($\vec{d}$ = 0) to points away from (upper) and towards (lower) the slab center, where $\vec{a}$ and $\vec{c}$ are primitive lattice translation vectors.